TITLE: Ablation of hematopoietic stem cell derived adipocytes reduces tumor burden in syngeneic mouse models of high-grade serous carcinoma

ONE SENTENCE SUMMARY: Hematopoietic stem cell derived adipocytes may alter the peritoneal metabolic and immune environment to establish a metastatic niche and support ovarian cancer progression.

AUTHORS: Elizabeth R Woodruff[1*], Courtney A Bailey[1,2*], Francis To[1*], Vyshnavi Manda[3], Joanne K Maltzahn[4%], Timothy M Sullivan[4%], Meher P Boorgula[5,6], Maria Sol Recouvreux[7], Ruby Vianzon[8^], Bogi Conrad[8^], Kathleen M Gavin[8], Kimberly R Jordan[9], Dwight J Klemm[4,10], Sandra Orsulic[7], Benjamin G Bitler[1], Zachary L Watson[1#]

AFFILIATIONS:

1 Division of Reproductive Sciences, Department of Obstetrics & Gynecology, University of Colorado School of Medicine, Aurora, CO 80045, USA

2 Biomedical Engineering Program, University of Colorado Boulder, Boulder, CO 80309, USA

3 Department of Medicine, University of Colorado School of Medicine, Aurora, CO 80045, USA

4 Department of Pulmonary Sciences and Critical Care, University of Colorado School of Medicine, Aurora, CO 80045, USA

5 University of Colorado Cancer Center, University of Colorado Anschutz Medical Campus, Aurora, CO 80045, USA

6 Department of Biomedical Informatics, University of Colorado Anschutz Medical Campus, Aurora, CO 80045, USA

7 Departments of Obstetrics & Gynecology and Pathology, and the Jonsson Comprehensive Cancer Center, David Geffen School of Medicine at UCLA, Los Angeles, CA 90095, USA

8 Division of Geriatric Medicine, Department of Medicine, University of Colorado School of Medicine, Aurora, CO 80045, USA

9 Department of Immunology and Microbiology, University of Colorado School of Medicine, Aurora, CO 80045, USA

10 Geriatric Research, Education and Clinical Center, Rocky Mountain Regional Veterans Administration (VA) Medical Center, Aurora, CO 80045, USA

* **Co-First Authors: ERW, CAB, and FT contributed equally**

% Tertiary authors JKM and TMS contributed equally

^ Tertiary authors RV and BC contributed equally

Corresponding Author

Zachary L. Watson

Division of Reproductive Sciences

Department of Obstetrics & Gynecology

12700 E. 19th Ave., MS8613

Aurora, CO 80045

Phone: (303) 724-8682

Fax: (303) 724-3512

zachary.watson@cuanschutz.edu

Word count: 8200

Figure count: 5

Table count: 3

Supplemental figure count: 11

Supplemental table count: 5

ABSTRACT: Hematopoietic stem cell-derived adipocytes (HSCDAs) are an adipose subtype derived from myeloid precursors that are distinct from conventional mesenchymal adipocytes (CMAs). We hypothesized that HSCDAs promote high grade serous carcinoma (HGSC), the most common form of ovarian cancer. Despite similar rates of differentiation, primary human HSCDAs from female donors showed marked transcriptional differences from CMAs, including downregulation of cell cycle and upregulation of lipid metabolic pathways. HSCDAs secreted greater amounts of inflammatory cytokines than CMAs. We also conducted two independent tumor studies using ID8 and SO syngeneic HGSC murine models in immunocompetent mice that were either HSCDA Proficient (HSCDA-Pro; can make both adipocyte subtypes) or Deficient (HSCDA-Def; can only make CMAs). Tumor burden trended lower in HSCDA-Def mice in both models. Relative to HSCDA-Pro mice, omental ID8 tumors from HSCDA-Def mice downregulated transcription of multiple metabolic pathways that were enriched in human HSCDA cells *in vitro*, suggesting that ablation of HSCDAs altered the tumor metabolic environment. Compared to HSCDA-Pro mice, tumors from HSCDA-Def mice had lower densities of dendritic cells (DC) and natural killer (NK) cells, as well as fewer DCs, NKs, and B-cells in proximity to tumor cells. Our data suggest that HSCDAs alter the peritoneal immune and metabolic environment to support HGSC progression.

MAIN TEXT:

INTRODUCTION

Most ovarian cancers are of the high-grade serous subtype (high grade serous carcinoma; HGSC) [1]. HGSC preferentially invades visceral adipose tissues (VAT) such as the omentum [2-5], a complex apron-like fold of the visceral peritoneum that lies across the anterior aspect of the intestines. It is primarily composed of adipocytes surrounded by a mesothelial layer but also contains vasculature and “milky spots,” small tertiary lymphoid aggregates that may be innervated by sympathetic nervous system fibers [6-8]. Omental tumors are often the largest abdominal tumors in women with ovarian cancer, suggesting that the microenvironment of the omentum is highly conducive to HGSC cell invasion and proliferation. Adipocytes actively enhance HGSC metastasis through several mechanisms, including but not limited to: (a) secretion of inflammatory cytokines, such as IL-8, promoting HGSC migration and invasion, (b) providing energy to HGSC cells through direct lipid transfer, and (c) stimulating upregulation of fatty acid binding protein 4 (FABP4), fatty acid translocase (CD36), and other regulatory proteins of fatty acid transport and lipid metabolism [9-11].

During aging, visceral adiposity increases through the enlargement of existing adipocytes (hypertrophy) and/or *de novo* production of new adipocytes (hyperplasia). Adipocytes were previously proposed to arise exclusively from mesenchymal precursors; however, a 2006 murine bone marrow transplant study demonstrated that a subset of circulating myeloid cells home to adipose tissue, become resident, and terminally differentiate into adipocytes [12]. These cells were termed hematopoietic stem cell-derived adipocytes (HSCDAs) in a recent publication [13] to distinguish them from conventional mesenchymal-derived adipocytes (CMAs). Later human studies in 2015 and 2016 confirmed the presence of HSCDAs in humans [14, 15]. Ryden et al. isolated mature white adipocytes from recipients of bone marrow transplants (BMT) and evaluated them for donor and recipient DNA. Up to 27% of purified adipocytes were derived from donor cells and the fraction of donor-derived adipocytes was positively correlated with time since transplant [14]. Gavin et al. performed a similar study and found that up to 35% of mature adipocytes were generated from donor cells in BMT recipients, and the proportion of donor DNA was positively correlated with elapsed time post-transplant [15]. These two independent studies both confirmed human HSCDA existence and demonstrated that their proportion of total adipose cells increases with age.

Subsequent studies developed methods to isolate and differentiate human primary adipocyte precursors into HSCDA and CMA populations, and also established an innovative murine model for HSCDA ablation [13, 16-18]. These studies demonstrated that mouse HSCDAs accumulated with age and occurred in significantly higher numbers in female versus male mice. Transcription analysis showed that HSCDAs differ from CMAs by upregulation of inflammatory gene expression and decreased expression of leptin and lipid oxidation pathways [19]. Of key relevance to menopause and HGSC, mouse HSCDA production was found to be enhanced by models of "pseudomenopause" such as ovariectomy and estrogen receptor alpha knockout. HSCDA production in ovariectomized mice was attenuated by estradiol replacement, demonstrating that the ovarian hormone is necessary and sufficient for the constraint of HSCDA production. In agreement with prior anatomical studies, HSCDA accumulation in these mice was higher in visceral adipose tissue (VAT) and gonadal adipose tissue (GAT) compared to subcutaneous adipose tissue (SAT) depots [17]. Finally, depletion of HSCDAs in mice did not alter the quantities of tissue-resident immune cells in GAT or SAT depots; however, HSCDA depleted mice were found to have increased circulating leptin levels, indicating that the presence or absence of HSCDAs may alter lipid homeostasis [13].

Numerous studies have surveyed the effects of adipocytes on ovarian cancer progression, metastasis, and metabolism, but to date, none have compared the distinct influences of HSCDAs and CMAs. Given their presence in humans and their characteristics in murine models, we predicted that HSCDAs would exhibit differential transcription and secretion than CMAs, and that HGSC tumors would show differential growth and spread in mice that had been ablated of HSCDAs.

RESULTS

Human hematopoietic and mesenchymal precursor cells are equally capable of adipogenic differentiation

Prior studies have successfully differentiated mouse hematopoietic and mesenchymal precursor cells into HSCDAs and CMAs, respectively [13]. To develop a complementary human *in vitro* model, researchers collected human subcutaneous adipose biopsies, which were dissociated, sorted by fluorescence activated cell sorting (FACS) into mesenchymal and hematopoietic populations, and then cryopreserved for subsequent adipogenic differentiation. For this study, with informed consent for secondary use, we acquired adipose

progenitors from human female donors. As the original human subjects research that collected these tissues is in the preprint stage [18], with permission from the authors, we have included information about study participants, adipose biopsy collection and processing, flow sorting, and subsequent culture in our Materials and Methods. The FACS gating strategy is shown in **Supplementary Fig. S1**. Study participant data, including age, menopause status, height, total mass, and fat mass are shown in **Table 1**.

To determine if mesenchymal and hematopoietic cells differentiated at the same rate, we acquired daily brightfield images of differentiating cells from three independent human donors (Donors 1-3). **Fig. 1A-C** shows cells from each donor at the pre-differentiated state (day 0, D0), mid-differentiation (day 8, D8), and at the end of the differentiation process (day 14, D0). At D0, precursor cells were confluent. By D8, all cells began to show accumulation of lipid droplets, which were extensive by D14 in both Donor 1 and Donor 3 **(Fig. 1A, C)**. Both mesenchymal and hematopoietic cells from Donor 2 showed less extensive lipid accumulation **(Fig. 1B)**. The full set of daily images (D0-D14) for all three donors are shown in **Supplementary Fig. S2-S4**.

To further compare the rate of adipogenic differentiation, we isolated RNA from donor cells collected pre-differentiation (D0) and post-differentiation (D14). We then performed RT-qPCR to determine if adipose gene expression (*FABP4*, *FASN*, and *PPARG*) was similar between HSCDAs and CMAs. All precursor cells from all three donors showed low expression of target genes at D0 **(Fig. 1D, G, J)**. Expression was higher at D14 **(Fig. 1E, H, K)**. Gene expression and fold-increases varied by donor, but there was no observed trend of consistently greater gene expression, or of increase in gene expression, from either HSCDAs or CMAs. Illustrating this point, *FASN* fold increases were not statistically significant between HSCDAs and CMAs for Donor 1 or for Donor 3, while *FABP4* and *PPARG* fold-increases were higher in Donor 1 CMAs than HSCDAs, but higher in Donor 3 HSCDAs than CMAs **(Fig. 1F, I, L)**. Notably, both HSCDAs and CMAs from Donor 2 showed lower levels of gene expression and fold-increase **(Fig. 1F, I, L)**, which is consistent with the images showing less extensive lipid accumulation **(Fig. 1B)**. Overall, we conclude that the extent of differentiation is donor dependent but does not appear to be precursor cell type dependent. Both hematopoietic and mesenchymal cells were capable of similar adipogenic differentiation within the observed time frame.

Cultured human HSCDAs and CMAs exhibit differential transcription

Prior transcriptomic data from murine-derived HSCDAs and CMAs showed that the former exhibit a highly inflammatory transcriptional profile compared to the latter, including increased mRNA expression of *Cxcl10*, *Mcp1*, *Il6*, and *Cxcl1* [19]. We hypothesized that *in vitro* cultured human HSCDAs would also exhibit unique transcriptional profiles. We performed RNA-Seq on matched HSCDA/CMA pairs (post-differentiation at D14) from three independent donors (Donors 1-3) **(Fig. 2A)**. Principal component analysis (PCA) showed that HSCDA and CMA cells from Donor 1 and Donor 3 clustered together, while HSCDAs and CMAs did not cluster for Donor 2 **(Fig. 2B)**. Next, we examined differential gene expression (DGE, **Fig. 2C**) and performed over-representation analysis (ORA) for Hallmark pathways. Multiple cell cycle pathways decreased in human HSCDA cells, including E2F Targets, Mitotic Spindle, and G2M Checkpoint **(Fig. 2D)**. The heatmap for Hallmark E2F targets showed that HSCDAs, regardless of donor, clustered separately from CMAs **(Fig. 2E)**. Functional gene set enrichment analysis (fGSEA) recapitulated downregulation of these three pathways **(Fig. 2F)**. fGSEA also revealed enrichment in HSCDAs for multiple Hallmark metabolic pathways, including Oxidative Phosphorylation, Adipogenesis, and Fatty Acid Metabolism **(Fig. 2F-I)**. Overall, these data show that, despite variability in gene expression and differentiation from specific donors, HSCDAs exhibit a unique transcriptional profile from CMAs, including differences in cell cycle and metabolic pathways.

Cultured human HSCDAs secrete greater amounts of inflammatory cytokines

While we did not observe transcriptional differences in inflammatory cytokines that were seen in mouse HSCDAs [19], we hypothesized that secretion may differ between human HSCDAs and CMAs. We analyzed conditioned media from paired HSCDAs and CMAs obtained from six independent human female donors (Donors 4-9) using a multiplex ELISA for 10 cytokines (IFN-γ, IL-1β, IL-2, IL-4, IL-6, IL-8, IL-10, IL-12p70, IL-13, and TNF-α). HSCDAs exhibited increased IL-6 and IL-8 secretion, with four donors producing higher concentrations of IL-6 and five donors producing higher concentrations of IL-8 compared to CMAs **(Fig. 3A-F)**. The remaining cytokines were not detected within the range of the assay. Averaged across all six donors, HSCDA media contained 5.7-times the concentration of IL-6, and 6.7-times the concentration of IL-8, compared to paired CMA media.

Because inflammatory cytokine secretion from adipocytes can influence HGSC progression [10], and HSCDAs secreted more IL-6 and IL-8 **(Fig. 3A-F)**, we next explored if cultured HGSC cells directly respond to

IL-6 and/or IL-8 exposure. Using RT-qPCR to assay mRNA expression of IL-6 receptors (*IL6R* and *IL6ST*) and IL-8 receptors (*CXCR1* and *CXCR2*) in PEO1 cells (*TP53-/-*, *BRCA2*-mutant), we observed robust expression of *IL6ST*, but low or no expression of the other receptors **(Fig. 3G)**. We then used flow cytometry to examine surface protein expression. In concordance with RT-qPCR, we found that over 80% of PEO1 cells expressed IL6ST, but very few cells expressed IL6R, CXCR1, or CXCR2 **(Fig. 3H** with representative flow gating shown in **Supplementary Fig. 5-6)**. We then incubated PEO1 cells directly in a high dose (50 ng/mL) of recombinant IL-6, IL-8, or both for 15 minutes or 1 hour and performed immunoblot for resultant intracellular signaling (phosphorylated STAT3 for IL-6; phosphorylated ERK1/2 for IL-8). At 15 minutes, we observed that phosphorylation of STAT3 at Y705 occurred in response to IL-6 alone and in combination with IL-8 **(Fig. 3I)**. However, at 1 hour, no p-STAT3 was observed **(Fig. 3J)**, indicating a transient response. We did not observe any changes to total STAT3, p-ERK1/2, or the β-actin loading control under any treatment or time point in PEO1 cells. To determine if PEO1 cells could respond to the range of IL-6 concentration observed in HSCDA conditioned media **(Fig. 3A-F)**, we incubated the cells for 15 minutes in a range of IL-6 doses from 5 pg/mL to 50 ng/mL **(Fig. 3K)**. By densitometry analysis of p-STAT3 bands, we observed increasing phosphorylation from 50 pg/mL upward. We performed parallel experiments in two additional HGSC cell lines, OVCAR4 (*TP53-/-*, *BRCA1/2* wild-type) and OVCAR8 (*TP53-/-*, *BRCA1/2* wild-type*, ERBB2* mutant, *KRAS* mutant, *CTNNB1* mutant) **(Supplementary Fig. S7)**. We observed comparable results in all experiments, including RNA and protein expression of receptors **(Supplementary Fig. S7A-C)**. We also observed upregulation of p-STAT3 in these lines in response to IL-6 at 15 minutes (and across multiple doses), but not at 1 hour **(Supplementary Fig. S7D-I)**.

Since we observed that HSCDAs secrete greater amounts of inflammatory cytokines than CMAs with the potential to drive a signaling response in HGSC cells, we incubated HSCDA and CMA media from four independent human female donors (Donors 6-9) in triplicate on PEO1 cells for 24 h and then analyzed protein expression and phosphorylation by reverse phase protein array (RPPA) **(Fig. 3L-R)**. The heatmap **(Fig. 3L)** shows proteins that were up- or down-regulated consistently across all four donors, including upregulated fibronectin (detailed in **Fig. 3M**), glyceraldehyde 3-phosphate dehydrogenase (GAPDH), and tissue transglutaminase 2 (TG2). As well as increased serine phosphorylation of multiple kinases, including AKT1-pS473, AKT2- pS474, and p21-activating kinase 4. Consistently downregulated proteins in HSCDA media,

relative to cells in CMA media, included multiple tumor suppressors such as the regulatory p85 subunit of PI3K (PI3K-p85), protein tyrosine phosphatase non-receptor type 12 (PTPN12), programmed cell death protein 4 (PDCD4), and glycogen synthase kinase 3 beta (GSK3β) (detailed in **Fig. 3N**). Notably, while phosphorylated forms of PAK4 **(Fig. 3O)** and AKT2 **(Fig. 3Q)** were found at higher levels, the total forms of these proteins **(Fig. 3P,R)** were not differentially expressed between treatment groups, highlighting specific differences in serine phosphorylation in the absence of overall protein changes. Overall, these data indicate increased inflammatory secretion from HSCDAs, with the potential to alter protein signaling and expression in HGSC cells, although factors other than cytokines may be involved in responses of longer duration.

Ablation of HSCDAs attenuates tumor burden in two independent syngeneic murine models of HGSC

We showed that HSCDAs secrete greater amounts of inflammatory cytokines IL-6 and IL-8 than CMAs, and that paracrine signaling in conditioned media alters protein expression and phosphorylation in HGSC cells **(Fig. 3)**. Both IL-6 and IL-8 have been shown to increase the metastatic and invasive capabilities of HGSC cells [10, 20, 21]. Adipocytes also alter the tumor metabolic environment and enhance tumor cell proliferation by providing energy through lipid transfer and stimulating HGSC cell fatty acid metabolism [9-11]. We therefore hypothesized that ablation of HSCDAs in mice may reduce tumor progression in syngeneic models of HGSC. To specifically ablate HSCDAs, irradiated recipient C57BL/6J mice were transplanted with hematopoietic stem cells (HSC) from donor mice in which a mature adipocyte-specific adiponectin gene promoter controls expression of an attenuated diphtheria toxin (DTA) gene [13]. This approach ablates any HSC that differentiates into an adipocyte by endogenous DTA expression, thereby specifically abrogating HSCDA production in the recipient mice. Importantly, CMAs are unaffected by myeloablation and transplant, as they are derived from host mesenchymal precursors that do not express the DTA construct. We refer to this mouse cohort as “HSCDA Deficient” or HSCDA-Def. Control mice were generated by transplanting HSCs from donor mice encoding a reporter gene but lacking DTA allowing the production of both HSCDAs and CMAs from hematopoietic and mesenchymal precursors, respectively. We refer to this mouse cohort as “HSCDA Proficient” or HSCDA-Pro.

Following a six-week recovery from HSC transplantation, HSCDA-Def and HSCDA-Pro mice were engrafted with ID8 (*Tp53-/-*, *Brca2-/-*, GFP+Luc+) cells by intraperitoneal (IP) injection **(Fig. 4A)**. Prior studies have extensively characterized this syngeneic murine model as being representative of human disease,

particularly in terms of its propensity to target and colonize the omentum before disseminating to other peritoneal sites [2, 22, 23]. Luciferase expression was examined by IP luciferin injection and live imaging at 7, 21, and 35 days after cell injection. Total flux and percent change in flux (relative to 7 days post-ID8 injection) were similar between HSCDA-Pro and HSCDA-Def mice **(Fig 4B-C)**. 39 days post-ID8 injection, tumor-bearing mice were euthanized, and necropsy was performed to assess tumor burden and collect specimens for downstream analyses of the tumor and peritoneal environment. While not statistically significant, average total omentum weight **(Fig. 4D)** strongly trended lower in HSCDA-Def mice compared to HSCDA-Pro mice (0.047 g vs 0.063 g; p=0.0921). The average number of disseminated tumor nodules **(Fig. 4E)** within the mesentery and other peritoneal locations was nearly significantly reduced in HSCDA-Def mice (24.5 vs. 35.9; p=0.0566). The average total mass per mouse of these tumor nodules **(Fig. 4F)** was significantly lower in HSCDA-Def mice (0.089 g vs. 0.125 g; p=0.0484). Representative necropsy images of the peritoneal space, including GFP+ omenta and disseminated tumors are shown in **Supplementary Fig. S8**.

Given the reduced overall tumor burden in HSCDA-Def mice, we performed immunohistochemistry (IHC) on omental tumor sections to determine if tumor cell proliferation was affected by HSCDA status. Representative brightfield images of Ki67 (proliferation) are shown in **Supplementary Fig. S9**. Consistent with reduced tumor burden, the percentage of Ki67 positive tumor cells strongly trended lower (p=0.0544) in HSCDA-Def mice (average = 8.4%) than in HSCDA-Pro mice (average = 11.1%) **(Fig. 4G)**. These data demonstrate that HSCDA-Def had slowed tumor proliferation, suggesting that the peritoneal adipose environment was less conducive to tumor growth. To examine the peritoneal adipokine milieu of tumor-bearing mice, we collected a portion of ascites fluid during necropsy. Cells were removed by centrifugation, and adipokine concentrations in the supernatant were analyzed using a multiplex ELISA for mouse BDNF, IL-1β, IL-6, IL-10, Insulin, Leptin, MCP-1, and TNF-α. All adipokines were detected within the assay range. While IL-6 trended higher in HSCDA-Def mice, no differences in measured adipokine concentrations reached statistical significance **(Supplementary Fig. S10)**.

As further confirmation of the effects of HSCDA ablation, we performed a follow-up tumor study in HSCDA-Pro and HSCDA-Def mice using the “SO” model [a kind gift from the Sandra Orsulic laboratory, UCLA]. SO cells are *Tp53-/-*, *Brca1/2* wild-type, $Hras^{V12}$ and *Myc* amplified. After an 8-week recovery of mice from myeloablation and bone marrow transplant, SO cells were implanted by IP injection into recipient C57BL/6J mice. The SO model is extremely aggressive, so only 20,000 cells were injected per mouse (compared to 5

million ID8 cells per mouse). Accordingly, mice formed large solid omental and peritoneal tumors very rapidly, leading to the euthanization of the mice within 20 days post-SO injection. Consistent with the ID8 model, we observed non-significant reduction in omental tumor weight (p=0.29), as well as a strong trend toward reduced number (p=0.06) and mass (p=0.08) of non-omental peritoneal tumors in HSCDA-Def mice **(Supplementary Fig. S11)**. While the effects are modest in magnitude, the ID8 and SO studies collectively demonstrate that HSCDA ablation reduces overall intraperitoneal tumor burden in two independent syngeneic HGSC models.

HSCDA ablation alters gene transcription and the tumor immune microenvironment in ID8 tumor-bearing mice

We next assessed the HSCDA-dependent transcriptome and tissue architecture. We conducted RNA-Seq of ID8 omental tumors from HSCDA-Pro (n=4) and HSCDA-Def (n=4) mice to characterize the transcriptional profiles of the tumor microenvironment. We first assessed transcription of a tdTomato transgene, expressed specifically by donor HSCs in all recipient mice, as a measure of donor cell engraftment and expansion into recipient tissues (in this case, within the omentum). We found that tdTomato expression, as a percentage of total transcriptional counts per mouse, was lower in HSCDA-Def mice **(Fig. 5A)**. We next examined overall endogenous gene expression. PCA showed broad clustering of HSCDA-Pro (blue) and HSCDA-Def (red) groups **(Fig. 5B)**. DGE analysis revealed a trend toward upregulation of gene expression in HSCDA-Def mice relative to HSCDA-Pro controls **(Fig. 5C)**. fGSEA analysis identified multiple differentially regulated Hallmark pathways **(Fig. 5D)**. Notably, three pathways we identified as enriched in human HSCDA cultures – Fatty Acid Metabolism, Oxidative Phosphorylation, and Adipogenesis **(Fig. 2F)** – were depleted in HSCDA-Def mice **(Fig. 5E-G)**, suggesting that HSCDA depletion had altered the metabolic environment of the omentum.

fGSEA analysis also revealed the depletion of multiple immune-related Hallmark pathways, including Allograft Rejection, Inflammatory Response, and IL-2 STAT5 Signaling **(Fig. 5H-J)**. We then performed multispectral IHC (mIHC) on omental tumors to assess whether HSCDA status affected the tumor immune microenvironment. Tissue sections were stained using two separate panels of antibodies, both of which included staining for nuclei (DAPI) and the transcription factor WT1, which identifies ID8 tumor cells. The “innate” panel **(Table 2)** detected myeloid cells including dendritic cells (DC), natural killer cells (NK), macrophages, and subpopulations of myeloid derived suppressor cells (MDSCs). The “adaptive” panel **(Table 3)** detected lymphoid

cells including B-cells and several subtypes of T-cells. After tissue and cell segmentation, cell densities were quantified in regions of interest. We found that the densities of DCs (CD11c+) and NKs (CD49b+/CD31-) were significantly lower in omental tumors from HSCDA-Def mice compared to HSCDA-Pro mice **(Fig. 5K)**. Following the cell density analysis, we performed spatial analysis to calculate the number of each immune cell type within 50 microns of WT1+ tumor cells. Within this radius, the numbers of B-cells (B220+), DCs (CD11c+), and NKs (CD49b+/CD31-) were reduced in the omental tumors of HSCDA-Def mice compared to HSCDA-Pro mice **(Fig. 5L)**. These analyses show that HSCDA ablation affected not only tumor burden and bulk transcription but also the tumor immune microenvironment.

DISCUSSION

Human data suggest that the proportion of HSCDAs increases over time [15]. In mouse models, HSCDAs preferentially accumulate in VAT and GAT depots, and their production is inversely correlated with estrogen signaling [17]. Crucially, most ovarian cancer diagnoses occur post-menopause [24], and the aged peritoneal microenvironment can be highly conducive to ovarian cancer progression [25]. We hypothesized that HSCDAs may promote HGSC progression by establishing a pro-tumor niche within VAT, such as the omentum, a site of particularly high HGSC dissemination in human cases.

Human hematopoietic and mesenchymal adipose precursors are equally competent for adipogenic differentiation **(Fig. 1** and **Supplementary Fig. S2-S4)**; however, human HSCDAs have a distinct transcriptional profile compared to CMAs, characterized by the downregulation of Hallmark cell cycle pathways and upregulation of multiple metabolic pathways, including Oxidative Phosphorylation, Adipogenesis, and Fatty Acid Oxidation **(Fig. 2)**. ELISA of adipocyte conditioned media showed that human HSCDAs secrete higher amounts of IL-6 and IL-8 than CMAs **(Fig. 3)**. Our RPPA data **(Fig. 3L-R)** indicated that PEO1 cells in HSCDA media, relative to CMA media, exhibit upregulated tissue transglutaminase 2, which has been associated with epithelial-to-mesenchymal plasticity (EMP) in ovarian cancer [26, 27], as well as fibronectin, which is broadly associated with EMP in multiple cancer types [28]. Serine phosphorylation was also elevated in these cells, including pro-survival AKT1, AKT2, and PAK4, a group II serine/threonine protein kinase that can regulate cytoskeletal remodeling [29, 30] and Wnt/β-catenin signaling [31]. Interestingly, we observed that PEO1 cells cultured in HSCDA conditioned media exhibited downregulated GSK3β, a tumor suppressor and negative regulator of

Wnt/β-catenin signaling. Other downregulated tumor suppressors included PTPN12, a tyrosine phosphatase that regulates PTEN and AKT signaling and suppresses the migration of ovarian cancer cells [32, 33], and PDCD4, a pro-apoptotic tumor suppressor with clinical significance in gliomas and colorectal cancers [34, 35].

While adipocyte-derived IL-6 and IL-8 have been shown to promote ovarian cancer survival, metastasis, and chemoresistance [10, 36], our data show that PEO1, OVCAR4, and OVCAR8 cells in culture express low levels of IL-6 receptor (IL6R) and IL-8 receptors (CXCR1 and CXCR2) **(Fig. 3** and **Supplementary Fig. S7)**. It is therefore likely that additional signaling mechanisms regulate the observed differences in HGSC cell proliferation and protein expression in HSCDA media. Prior studies have shown that exosomes from human omentum conditioned media can increase the proliferative and invasive capacity of ovarian cancer cells [37], and microRNAs from adipose tissue-derived exosomes can regulate gene expression in non-adipose tissues [38, 39]. Both PTPN12 and PDCD4, tumor suppressors that were downregulated in PEO1 cells in HSCDA media **(Fig. 3)**, are regulated by microRNA miR-503 [40, 41]. Future work examining the contribution of exosome-derived factors, including microRNAs, may reveal additional mechanisms for our observations.

Results from our *in vivo* studies in two independent syngeneic HGSC models showed that ablation of HSCDAs moderately reduced overall tumor burden, particularly by lowering the number and mass of metastatic tumor nodules in the mesentery and other peritoneal sites **(Fig. 4** and **Supplementary Fig. S8** and **S11)**. Reduced Ki67 positivity in ID8 tumor cells from HSCDA-Def mice suggests that lower tumor burden may be due to slowed proliferation **(Fig. 4G** and **Supplementary Fig. S9A-B)**. Bulk RNA-Seq of ID8 omentum tumors revealed that HSCDA ablation caused a reduction in Hallmark pathways Fatty Acid Oxidation, Oxidative Phosphorylation, and Adipogenesis **(Fig. 5D-G)**. These pathways were upregulated in human HSCDA cultures **(Fig. 2F-I)**, suggesting that HSCDA ablation contributed to loss of their expression in mice. Combined with the observed reduction in tumor burden and reduced Ki67, these data suggest that the peritoneal metabolic environment of HSCDA-Def mice was less supportive of tumor cell metastasis and growth **(Fig. 4H** and **Supplementary Fig. S9)**. Further animal studies are underway to characterize the visceral metabolic environment of HSCDA-Pro and HSCDA-Def mice in the absence of tumor cells and to characterize the tumor metabolic microenvironment of engrafted solid tumors and free fatty acid composition of ascites fluid.

RNA-Seq of omentum ID8 tumors also revealed downregulation of multiple immune-related pathways **(Fig. 5H-J)** HSCDA-Def mice relative to HSCDA-Pro mice. Omental tumors in HSCDA-Def mice showed reduced

density of dendritic cells and natural killer cells, as well as fewer DCs, NKs, and B-cells within a 50 μm radius of tumor cells **(Fig. 5K-L)**. A caveat of these findings is the difference in tdTomato expression between HSCDA-Pro and HSCDA-Def omentum tumor samples **(Fig. 5A)**, which may reflect a difference in engraftment of hematopoietic cells. However, significant differential engraftment would likely result in an overall difference in all myeloid populations, which was not observed. In terms of function, innate immune cells such as NKs and DCs can directly target malignant cells and broadly promote the recruitment of adaptive immune cells, and it has been proposed that B-cells also promote the HGSC anti-tumor response [42]. However, tumor-promoting roles have also been described for each of these cells. For example, tumor microenvironment components can suppress NK cell cytotoxicity and induce angiogenesis [43]. In a study of murine adenocarcinoma and melanoma, NK cells rapidly lost effector functions after entering the tumor environment [44]. Additionally, regulatory B-cells can suppress immune response through the production of anti-inflammatory cytokines [45, 46]. Further exploration is needed to characterize the populations of tumor infiltrating DCs, NKs, and B-cells, and whether the balance of pro- and anti-tumor cells can be shifted by the presence of HSCDAs.

In conclusion, we present the first study characterizing human HSCDAs in the context of ovarian cancer, as well as two independent *in vivo* tumor studies comparing HSCDA-Def and HSCDA-Pro mice. Our results suggest HSCDAs are important contributors to ovarian cancer progression that may alter the peritoneal immune and metabolic environment to establish a metastatic niche and promote disease progression. Future studies are underway to shed light on specific mechanisms. Use of genetically engineered murine models that develop spontaneous cancers [47, 48] may prove useful, as they give a longer period of time for the pro-tumorigenic properties of HSCDAs to become apparent. The current models, while showing trends and some significant differences, are limited to an acute tumor-adipose exposure time of only a few weeks. Despite this limitation, our findings in mice raise the possibility of specifically targeting HSCDAs in humans as a method of reducing metastatic tumor burden.

MATERIALS AND METHODS

HGSC cell culture

PEO1 (RRID:CVCL_2686), OVCAR4 (RRID:CVCL_1627), and OVCAR8 (RRID:CVCL_1629) were obtained from the Gynecologic Tissue and Fluid Bank (GTFB) at the University of Colorado and were authenticated at the University of Arizona Genomics Core using short tandem repeat DNA profiling. Cells were confirmed free of mycoplasma using MycoLookOut PCR (Sigma) last evaluated on July 12, 2024. Standard culture condition for these lines is 37 °C in 5% CO_2 in RPMI 1640 supplemented with 10% fetal bovine serum (FBS) and 1% penicillin/streptomycin.

Study Participants (reproduced with author permission from [18])

The study was approved by the Colorado Multiple Institutional Review Board (COMIRB) and written informed consent was obtained from all participants. All procedures took place at the Clinical and Translational Research Center (CTRC) at the University of Colorado Anschutz Medical Campus (CU-AMC). Samples were obtained from participants enrolled in NCT02654925, NCT02758431, and NCT04043520. Participants were healthy males and females either 20-50 or >50-75 years of age (y). Older women were postmenopausal as identified by no menstrual cycles within the last 12 months and confirmed by follicle-stimulating hormone (FSH) ≥ 30 mIU/mL. Premenopausal women were not currently pregnant or lactating. Inclusion criteria included a BMI between 20 and 40 kg/m^2. Exclusion criteria included current (within the last 6 months) use of any hormone replacement or hormonal contraceptive, use of glucose lowering medication and diagnosis of type 2 diabetes or uncontrolled metabolic disorders.

Adipose tissue biopsy collection and processing (reproduced with author permission from [18])

The skin and subcutaneous abdominal adipose tissue directly adjacent to the umbilicus underwent local numbing with 1% lidocaine without epinephrine, after which the adipose tissue samples were obtained using a modified Coleman's manual vacuum ("mini liposuction") technique. A small incision was made, followed by infiltration of the adipose tissue with ~30- 50 mL of 0.15% tumescent lidocaine solution in 0.9% normal saline using a Coleman infiltration cannula. Approximately one to three grams of adipose tissue was removed using a Coleman aspiration

cannula. Adipose tissue was rinsed with collection buffer (Krebs-Ringers-HEPES (KRH), 2.5 mM glucose, 200 nM adenosine, pH 7.4) and obvious blood vessels and clots removed. 250-500 mg was flash frozen in liquid nitrogen and stored at -80 °C. Remaining tissue was transported to the laboratory where collection buffer was replaced with prewarmed digestion buffer (KRH, 2.5 mM glucose, 2% fetal bovine serum [FBS], 200 nM adenosine, 1mg collagenase/0.25 g tissue, pH 7.4). Tissue was digested for 30-60 minutes in a shaking water bath maintained at 37 °C. The resultant cell suspension was filtered through 250 µm mesh and digestion stopped with 1X volume of wash buffer (Hanks Balanced Salt Solution [HBSS] + 2% FBS + 200 nM adenosine). Samples were spun at 300 x *g* for 10 min, the floating adipocytes removed to a clean tube, and wash steps repeated. The stromal pellets were combined and spun at 500 x *g* for 10 min to pellet the cells. Here forward, all spins were at 500 x *g* for 10 min unless otherwise stated. The stromal cell pellet was resuspended in 10 mL Erythrocyte Lysis Buffer and incubated for 10 min on ice. Simultaneously, 1 mL of blood underwent red blood cell lysis. When applicable, adipose and blood samples were processed in parallel from here forward. After erythrocyte lysis, samples were spun and cell pellet resuspended in 1 mL wash buffer. Live cells were counted via trypan blue detection on a Cellometer X1 (Nexcelom Bioscience LLC, Lawrence, MA) cell counter.

Fluorescence activated cell sorting (FACS) of processed adipose biopsies (reproduced with author permission from [18])

After counting, cells were spun and resuspended at a concentration of 1 x 10^6 cells/100µL in wash buffer. Human TruStain FcX was added at 5µL/100µL cell suspension and cells incubated on ice for 10 min. All lineage antibodies were added at 5µL per million cells in 100 µL staining volume (or 0.25µg/10^6 cells) and mixed gently. Samples were incubated on ice in the dark for 25 min. Following incubation, samples were spun, the supernatant aspirated, and the cell pellet resuspended in wash buffer. After removal of the second supernatant, the cells were resuspended in flow buffer (HBSS + 5% FBS + 200 nM adenosine, pH 7.4) with volumes adjusted to 500µL – 1mL for cell sorting. DAPI was added to a final concentration of 1 mg/mL. Cell sorting was initiated within 15 minutes. Unstained cells, single color compensation beads and fluorescent minus one (FMO) controls were used. Antibodies are listed in the supplementary information of reference [18]. SVF cells were sorted using an Astrios cell sorter with Summit 6.3 software (Beckman Coulter, Fullerton, CA, USA). A 70 µm nozzle tip was used with a sheath pressure of 60 PSI and a drop drive frequency of approximately 95,000 Hz with an amplitude

of 15V. Manufacturer's protocols were followed to quality control and set up the sorter. The sheath fluid was IsoFlow. The sample and collection tubes were maintained at 10 °C using an attached recirculating water bath. To keep cells in suspension, the Astrios' SmartSampler sample station was set to maintain an agitation cycle of 5 seconds on and 8 seconds off. The sample flow rate was set to a pressure differential of <1.0 PSI. Sort mode was set to Purify 1. Appropriate signal compensation was set using single-color control samples. Cells were identified with the following surface markers: mesenchymal lineage cells, CD45NEG; conventional mesenchymal adipocyte precursor cells, CD45NEG/CD31NEG/CD29POS; hematopoietic Lineage, CD45POS; myeloid lineage, CD14POS; macrophages (ATM) & monocytes, CD14POS/HLA-DRPOS with divergent expression of CD206 (ATM CD206POS, monocytes CD206NEG); neutrophils, CD14POS, CD16POS, HLA-DRNEG, Siglec-8NEG; basophils, CD14NEG/Siglec-8POS; lymphocytes, CD14NEG/CD206NEG.

Expansion of sorted cells (reproduced with author permission from [18])

Sorted cells were gently vortexed and spun for 10 min at 500 x *g*. Cell pellets were resuspended in growth medium and conventional mesenchymal lineage cells were plated directly onto cell culture treated plastic plates for proliferation by standard techniques at a density of ~4,500 cells/cm2. Fresh growth media was applied the next day, and media changes took place every 2-3 days throughout the studies. Cells were grown to 70-80% confluence, detached with 30-60 min room temperature incubation in Accutase and passaged 1-2 additional times. Cells were frozen down in liquid nitrogen for use in future experiments. ATM/monocytes, neutrophils, and lymphocytes were each resuspended in 10 mL growth media at 40,000 cells/µL. Fibrinogen (60 µL, 5 mg/mL in 0.9% saline) was added, mixed gently and transferred to one well of a 96 well plate (per 400,000 cells) containing 1.4 µL of thrombin (50 U/mL) and the suspension mixed by gentle pipetting. Clots formed over 30–60 minutes and growth media was subsequently overlaid. Media was refreshed every 2-3 days throughout the study. Cells were recovered from the clots after 5-7 days. The culture medium was removed and matrices rimmed with a 27-gauge needle. The remaining liquid in the well was removed and 100 µL of digestion mix (75 µL growth medium + 23 µL bovine plasminogen (1.12 mg/mL) + 2µL urokinase (20 U/µL)) was added for 60 minutes at 37 °C, mixing by pipetting every 20 minutes. After digestion, cells were pelleted in a 1.5 mL tube at 500 x *g* for 10 minutes, resuspended in growth medium, and re-plated directly onto plastic into the same number of wells of a 96 well plate. All cells then underwent identical culture methodology to the mesenchymal lineage cells.

Primary preadipocyte culture, adipogenic differentiation, and conditioned media collection

Primary mesenchymal and myeloid-derived adipocyte precursors were grown in 15 cm tissue culture plates in Growth Media (GM): Alpha-MEM (Corning #10-022-CV) supplemented with 10% FBS (Gemini #100-106) and 0.1% penicillin/streptomycin (Sigma #P4333). Upon confluence, cells were differentiated for seven days in Complete Differentiation Media (CDM): DMEM/F12 (Corning #10-092-CV) supplemented with 33 μM D-biotin (Sigma #B4639), 17 μM pantothenate (Sigma #P5155), 1 μM rosiglitazone (Fisher #NC9331406), 0.5 mM 3-isobutyl-1-methylxanthine (IBMX; Sigma #I5879), 2 nM 3,3',5-triiodo-L-thyronine (T3; Sigma #T6397), 10 μg/mL transferrin (Sigma #T8158), and 100 nM insulin (Sigma #I9278). Cultures were then maintained for seven days in adipocyte maintenance media (AMM): DMEM/F12 supplemented with 33 μM D-biotin, 17 μM pantothenate, and 10 nM insulin (same suppliers as CDM). At the end of the seven-day AMM period, media was removed from adipocyte cultures. Cells were gently washed with PBS, and then media was replaced with fresh AMM. After a 24-hour incubation, conditioned media was collected for subsequent use.

Bulk RNA-Seq of human primary HSCDAs and CMAs

Total RNA was isolated from human primary HSCDA and CMA cultures using the RNeasy Plus kit (Qiagen). Library preparation and sequencing were performed by the University of Colorado Cancer Center Genomics Shared Resource (RRID:SCR_021984). Reads were analyzed by the University of Colorado Cancer Center Bioinformatics Core Facility (RRID:SCR_021983). RNA-Seq data were processed using the nf-core RNAseq pipeline (version 3.12.0; [49]). Briefly, Illumina adapters were removed using Cutadapt (version 3.4; [50]) as part of the trimgalore (0.6.7) package [51]. Reads were aligned using STAR (version 2.7.9a; [52]) to the human transcriptome (GRCh38, gene annotation from Ensembl release 104) and quantified using Salmon (version 1.10.1; [53]). Raw data with counts by gene was generated using tximport ([54]) on salmon quantified data. Normalized data was generated to counts per million [55]. Differential expression was calculated between sample groups using the limma R package [56]. Gene set enrichment analysis (GSEA) was performed using fold-change and the fgsea R package [57] with Hallmark gene sets from the Molecular Signatures Database [58], which were downloaded using the msigdbr R package. Raw and processed RNA-Seq data was deposited in the Gene Expression Omnibus (GSE277309).

Multiplex ELISA

For human cytokines in conditioned media, AMM was incubated on HSCDA or CMA cells for 24 h, then collected. The concentration of 10 cytokines (IFN-γ, IL-1β, IL-2, IL-4, IL-6, IL-8, IL-10, IL-12p70, IL-13, and TNF-α) in conditioned media was measured using the V-PLEX Proinflammatory Panel 1 Human Kit (Meso Scale Diagnostics #K15049D). For mouse adipokines, ascites fluid was collected from the peritoneal space of tumor-bearing HSCDA-Pro and HSCDA-Def mice using a needle and syringe. The supernatant was cleared of cells by centrifugation, and the concentrations of 8 adipokines (BDNF, IL-1β, IL-6, IL-10, Insulin, Leptin, MCP-1, and TNF-α) were measured in the supernatant using the U-PLEX Adipokine Combo 1 mouse kit (Meso Scale Diagnostics #K15299K).

Reverse-transcriptase quantitative PCR (RT-qPCR)

RNA was isolated from cells using the RNeasy Plus kit (Qiagen). mRNA expression was determined using SYBR green Luna One Step RT-qPCR Kit (New England BioLabs) on a Bio-Rad C1000 Touch thermocycler. Expression was quantified by the ΔCt method using target-specific primers and glyceraldehyde 3-phosphate dehydrogenase (*GAPDH*) control primers. mRNA-specific primers were designed to span exon-exon junctions to avoid the detection of genomic DNA. Primer sequences are shown in **Supplementary Table ST1**.

Flow cytometry for ovarian cancer cell cytokine receptor surface expression

One million HGSC cells grown in standard conditions (see above) were collected and resuspended in 100 µL of flow assisted cell sorting buffer (FACS buffer: Hank's Balanced Salt Solution [Corning #21-022-CV] with 2% FBS) and incubated in a 1:100 dilution of primary antibody for 20 minutes at 4 °C. Cells were then washed in 300 µL FACS buffer and centrifuged at 300 x *g* for 5 minutes. Cells were resuspended 300 µL FACS buffer and transferred to 5 mL tubes through 35 µm strainer caps (Falcon #352235). Full details of antibodies and isotype controls are given in **Supplementary Table ST2**. An Agilent Novocyte Penteon was used for detection and data were analyzed using FlowJo 10.8.1.

Immunoblotting

HGSC cells were seeded to sub-confluence in 10 cm dishes in standard media and allowed to settle overnight. Media was aspirated and cells were washed with PBS. Media was then replaced and supplemented with vehicle control, recombinant human IL-6 (BioLegend #570804), recombinant human IL-8 (BioLegend #574204), or both. Cells were incubated for 15 minutes or 1 hour, then rinsed and collected. Cell pellets were lysed in RIPA buffer (150 mM NaCl, 1% TritonX-100, 0.5% sodium deoxycholate, 0.1% SDS, 50 mM Tris pH 8.0) supplemented with protease inhibitor (Roche #11873580001) and phosphatase inhibitor (Roche #04906845001). Protein was separated by SDS-PAGE and transferred to PVDF membrane using the TransBlot Turbo (BioRad). Membranes were blocked in LI-COR Odyssey buffer (#927-50000) for use with LI-COR secondary antibody or in 2% BSA in TBS-T for use with HRP-linked secondary antibody for 1 hour at room temperature. Primary antibody incubation was performed overnight in blocking buffer at 4 °C. Membranes were washed 3 times for 10 minutes each in TBST (50 mM Tris pH 7.5, 150 mM NaCl, 0.1% Tween-20), then secondary antibodies were applied in blocking buffer for one hour at room temperature. Membranes were washed again 3 times for 10 minutes each in TBST. For LI-COR secondary antibody, bands were visualized using the LI-COR Odyssey Imaging System. For HRP-linked secondary antibody, membranes were incubated for 5 minutes in SuperSignal West Femto Maximum Sensitivity Substrate (Thermo #34095) and bands were visualized using a Syngene G:BOX. Densitometry of p-STAT3 bands was performed in ImageJ v1.54. Full details of primary and secondary antibodies are given in **Supplementary Tables ST3** and **ST4**.

Generation of HSCDA-Pro and HSCDA-Def Mice

The University of Colorado Institutional Animal Care and Use Committee (IACUC) approved all mouse studies. Tumor burden analysis was performed in bone marrow transplanted (recipient) wild-type C57BL/6J mice (Jackson Labs, strain #000664; RRID:IMSR_JAX:000664). HSCDA-Def mice were generated by transplanting recipient mice with bone marrow from transgenic donor mice in which an adipocyte specific adiponectin gene promoter (AdipoQ-Cre) controls the expression of an attenuated diphtheria toxin (DTA). HSCDA-Pro mice were transplanted with bone marrow from donor mice encoding AdipoQ-Cre but lacking DTA. Prior to transplant, 8- to 12-week-old female recipient mice were myeloablated by a split 12 Gy dose of X-ray irradiation (6 Gy doses split by 4 hours). Irradiated mice were rescued with retroorbital injection of 1 x 10^6 donor cells to reestablish the hematopoietic niche. Donor cells were obtained from fresh bone marrow of transgenic animals which can

produce mature adipocytes (AdipoQ-Cre) or lack mature adipocytes (AdipoQ-Cre-DTA). Adipocyte-deficient donor mice were generated by crossing animals in which Cre recombinase expression is directed by the adiponectin promoter (Jackson Labs #010803, B6;FVB-Tg(AdipoQ-cre)1Evdr/J; RRID:IMSR_JAX:010803) with mice in which the DTA gene is placed downstream of a floxed stop codon in the ROSA26 locus (Jackson Labs #010527, B6;129-Gt(ROSA)26Sortm1(DTA)Mrc/J; RRID:IMSR_JAX:010527). Cre-mediated excision of the stop codon initiates DTA expression and cell death, which is restricted to mature adipocytes by the adiponectin promoter. Adipocyte proficient donor mice are the result of the same cross, excluding the DTA gene. Recipient mice recovered from bone marrow transplantation for 6-8 weeks prior to tumor inoculation and experimentation protocols.

ID8 Animal Study

Six weeks after bone marrow transplant, 5 million ID8 cells (*Tp53-/-*, *Brca2-/-*, GFP-luciferase+,[59, 60]) were implanted into HSCDA-Pro and HSCDA-Def mice by intraperitoneal injection. Tumor development was monitored in all mice via biweekly In Vivo Imaging System (IVIS) scanning, as described previously [61]. 39-days post-ID8 cell injection, mice were euthanized, ascites fluid was collected, and necropsy was performed to assess tumor burden. All tumors were collected and weighed, including omentum tumors and disseminated tumor nodules within the mesentery and other peritoneal tissues.

SO Animal Study

Eight weeks after bone marrow transplant, 20,000 SO cells (*Tp53-/-*, *Brca1/2* wild-type, $Hras^{V12}$ and *Myc* transformed) were implanted into HSCDA-Pro and HSCDA-Def mice by IP injection. Mice were euthanized 20-days post-SO cell injection and necropsy was performed to assess tumor burden. All tumors were collected and weighed, including omentum tumors and disseminated tumor nodules within the mesentery and other peritoneal tissues.

Bulk RNA-Seq of ID8 Murine Omentum Tumors

Library preparation and sequencing were performed by the University of Colorado Cancer Center Genomics Shared Resource (RRID:SCR_021984). Reads were analyzed by the University of Colorado Cancer Center

Bioinformatics Core Facility (RRID:SCR_021983). RNA-Seq data were processed using the nf-core RNAseq pipeline (version 3.12.0; [62]). Briefly, Illumina adapters were removed using Cutadapt (version 3.4; [50]) as part of the trimgalore (0.6.7) package [51]. Reads were aligned using STAR (version 2.7.9a; [52]) to the Ensembl mouse transcriptome (GRCm39 release 104) and quantified using Salmon (version 1.10.1; [53]). Raw data with counts by gene was generated using tximport [54] on salmon quantified data. Normalized data was generated to counts per million [55]. Differential expression was calculated using the limma R package [56] comparing HSCDA-Def to the HSCDA-Pro sample groups. Volcano plot was generated with GraphPad Prism (ver. 10.2.3). Raw and processed RNA-Seq data was deposited in the Gene Expression Omnibus (GSE268528).

Multiplex Immunohistochemistry (mIHC) and Image Analysis

Tissues were formalin fixed for 48 hours at room temperature, embedded in paraffin blocks using a tissue processor, and sectioned at 4 microns onto charged glass slides. Slides were deparaffinized, heat treated in antigen retrieval buffer, blocked, and incubated with primary antibodies (**Tables 2 and 3**), followed by horseradish peroxidase (HRP)-conjugated secondary antibody polymer, and HRP-reactive OPAL fluorescent reagents. The slides were stripped between each consecutive staining cycle with heat treatment in antigen retrieval buffer. Whole slide scans were collected with PhenoImager HT v2.0.0 software using the 20x objective and a 0.5-micron resolution. Regions of interest (ROIs) were selected and re-scanned using the 20x objective and the multispectral imaging cube. Spectral references and unstained control images were measured and inForm software v3.0 was used to create a multispectral library reference. The multispectral images (.im3 files) were spectrally unmixed and analyzed with tissue segmentation, cell segmentation, and phenotyping using inForm software v3.0 (Akoya Biosciences). Exported data were compiled and summarized using PhenoptrReports (Akoya Biosciences). Full antibody details are given in **Supplementary Table ST5**.

Brightfield IHC and Image Analysis

Tissues were formalin fixed for 48 hours at room temperature, then paraffin embedded in blocks using a tissue processor and sectioned onto glass slides. All slides were de-identified and whole slide scans were collected on Akoya Biosciences Vectra 3 scanner using the 20x objective by the Human Immune Monitoring Shared Resource (RRID:SCR_021985). The slides were then analyzed on QuPath (v. 0.5.1 x64). ROIs were drawn to encompass

the whole tissue and background correction was done for H-DAB. For each stain, 4 ROIs were drawn for training sets and excluded from analysis for which cell and positive cell detect parameters could be identified. Cell detections were based on hematoxylin signal, with exclusions for minimum cell area and the inclusion of a median filter radius. Cell positivity was determined on DAB pixel intensity, and the percentage of positive cells was reported as the ratio of cells above a set DAB optical density mean to the total number of cells in the tissue. Data were exported and analyzed in GraphPad Prism 10 v. 10.3.1. The analyst was blinded to treatment group information until after the analysis was complete to avoid bias.

REFERENCES AND NOTES:

1. Jayson, G.C., et al., *Ovarian cancer.* Lancet, 2014. **384**(9951): p. 1376–88.
2. Gerber, S.A., et al., *Preferential attachment of peritoneal tumor metastases to omental immune aggregates and possible role of a unique vascular microenvironment in metastatic survival and growth.* Am J Pathol, 2006. **169**(5): p. 1739–52.
3. Swisher, E.M., et al., *Culprit or Bystander? The Role of the Fallopian Tube in "Ovarian" High-Grade Serous Carcinoma.* Cancer Discov, 2016. **6**(12): p. 1309–1311.
4. Dai, L., K. Song, and W. Di, *Adipocytes: active facilitators in epithelial ovarian cancer progression?* J Ovarian Res, 2020. **13**(1): p. 115.
5. Motohara, T., et al., *An evolving story of the metastatic voyage of ovarian cancer cells: cellular and molecular orchestration of the adipose-rich metastatic microenvironment.* Oncogene, 2019. **38**(16): p. 2885–2898.
6. Meza-Perez, S. and T.D. Randall, *Immunological Functions of the Omentum.* Trends Immunol, 2017. **38**(7): p. 526–536.
7. Cleypool, C.G.J., et al., *Sympathetic nerve tissue in milky spots of the human greater omentum.* J Anat, 2020. **236**(1): p. 156–164.
8. Clark, R., et al., *Milky spots promote ovarian cancer metastatic colonization of peritoneal adipose in experimental models.* Am J Pathol, 2013. **183**(2): p. 576–91.
9. Ladanyi, A., et al., *Adipocyte-induced CD36 expression drives ovarian cancer progression and metastasis.* Oncogene, 2018. **37**(17): p. 2285–2301.
10. Nieman, K.M., et al., *Adipocytes promote ovarian cancer metastasis and provide energy for rapid tumor growth.* Nat Med, 2011. **17**(11): p. 1498–503.
11. Nieman, K.M., et al., *Adipose tissue and adipocytes support tumorigenesis and metastasis.* Biochim Biophys Acta, 2013. **1831**(10): p. 1533–41.
12. Crossno, J.T., Jr., et al., *Rosiglitazone promotes development of a novel adipocyte population from bone marrow-derived circulating progenitor cells.* J Clin Invest, 2006. **116**(12): p. 3220–8.
13. Gavin, K.M., et al., *Hematopoietic Stem Cell-Derived Adipocytes Modulate Adipose Tissue Cellularity, Leptin Production and Insulin Responsiveness in Female Mice.* Front Endocrinol (Lausanne), 2022. **13**: p. 844877.
14. Ryden, M., et al., *Transplanted Bone Marrow-Derived Cells Contribute to Human Adipogenesis.* Cell Metab, 2015. **22**(3): p. 408–17.
15. Gavin, K.M., et al., *De novo generation of adipocytes from circulating progenitor cells in mouse and human adipose tissue.* Faseb j, 2016. **30**(3): p. 1096–108.
16. Gavin, K.M., et al., *Hematopoietic-to-mesenchymal transition of adipose tissue macrophages is regulated by integrin beta1 and fabricated fibrin matrices.* Adipocyte, 2017. **6**(3): p. 234–249.
17. Gavin, K.M., et al., *Ovarian Hormones Regulate the Production of Adipocytes From Bone Marrow-Derived Cells.* Front Endocrinol (Lausanne), 2018. **9**: p. 276.
18. Gavin, K.M., et al., *Adipogenic differentiation of hematopoietic lineage cells isolated from adipose tissue of humans.* bioRxiv, 2024: p. 2024.06.22.600230.
19. Majka, S.M., et al., *De novo generation of white adipocytes from the myeloid lineage via mesenchymal intermediates is age, adipose depot, and gender specific.* Proc Natl Acad Sci U S A, 2010. **107**(33): p. 14781–6.
20. Guo, Q.Y., et al., *IL-6 regulates epithelial ovarian cancer EMT, invasion, and metastasis by modulating Let-7c and miR-200c through the STAT3/HIF-1α pathway.* Med Oncol, 2024. **41**(6): p. 155.
21. Lee, J., et al., *Mitochondrial fission enhances IL-6-induced metastatic potential in ovarian cancer via ERK1/2 activation.* Cancer Sci, 2024. **115**(5): p. 1536–1550.
22. Etzerodt, A., et al., *Tissue-resident macrophages in omentum promote metastatic spread of ovarian cancer.* J Exp Med, 2020. **217**(4).
23. Krishnan, V., et al., *Omental macrophages secrete chemokine ligands that promote ovarian cancer colonization of the omentum via CCR1.* Commun Biol, 2020. **3**(1): p. 524.
24. Noone AM, H.N., Krapcho M, Miller D, Brest A, Yu M, Ruhl J, Tatalovich Z, Mariotto A, Lewis DR, Chen HS, Feuer EJ, Cronin KA, *SEER Cancer Statistics Review, 1975-2015*. 2018, National Cancer Institute, Bethesda, MD.
25. Harper, E.I., E.F. Sheedy, and M.S. Stack, *With Great Age Comes Great Metastatic Ability: Ovarian Cancer and the Appeal of the Aging Peritoneal Microenvironment.* Cancers (Basel), 2018. **10**(7).

26. Shao, M., et al., *Epithelial-to-mesenchymal transition and ovarian tumor progression induced by tissue transglutaminase.* Cancer Res, 2009. **69**(24): p. 9192–201.
27. Cao, L., et al., *Tissue transglutaminase links TGF-β, epithelial to mesenchymal transition and a stem cell phenotype in ovarian cancer.* Oncogene, 2012. **31**(20): p. 2521–34.
28. Lin, T.C., et al., *Fibronectin in Cancer: Friend or Foe.* Cells, 2019. **9**(1).
29. Abo, A., et al., *PAK4, a novel effector for Cdc42Hs, is implicated in the reorganization of the actin cytoskeleton and in the formation of filopodia.* Embo j, 1998. **17**(22): p. 6527–40.
30. Chetty, A.K., B.H. Ha, and T.J. Boggon, *Rho family GTPase signaling through type II p21-activated kinases.* Cell Mol Life Sci, 2022. **79**(12): p. 598.
31. Li, Y., et al., *Nucleo-cytoplasmic shuttling of PAK4 modulates β-catenin intracellular translocation and signaling.* Biochim Biophys Acta, 2012. **1823**(2): p. 465–75.
32. Villa-Moruzzi, E., *Tyrosine phosphatases in the HER2-directed motility of ovarian cancer cells: Involvement of PTPN12, ERK5 and FAK.* Anal Cell Pathol (Amst), 2011. **34**(3): p. 101–12.
33. Villa-Moruzzi, E., *PTPN12 controls PTEN and the AKT signalling to FAK and HER2 in migrating ovarian cancer cells.* Mol Cell Biochem, 2013. **375**(1-2): p. 151–7.
34. Gao, F., et al., *PDCD4 gene silencing in gliomas is associated with 5'CpG island methylation and unfavourable prognosis.* J Cell Mol Med, 2009. **13**(10): p. 4257–67.
35. Long, J., et al., *The mechanisms and clinical significance of PDCD4 in colorectal cancer.* Gene, 2019. **680**: p. 59–64.
36. Cardenas, C., et al., *Adipocyte microenvironment promotes Bclxl expression and confers chemoresistance in ovarian cancer cells.* Apoptosis, 2017. **22**(4): p. 558–569.
37. Qu, Q., et al., *Exosomes from Human Omental Adipose-Derived Mesenchymal Stem Cells Secreted into Ascites Promote Peritoneal Metastasis of Epithelial Ovarian Cancer.* Cells, 2022. **11**(21).
38. Ferrante, S.C., et al., *Adipocyte-derived exosomal miRNAs: a novel mechanism for obesity-related disease.* Pediatr Res, 2015. **77**(3): p. 447–54.
39. Thomou, T., et al., *Adipose-derived circulating miRNAs regulate gene expression in other tissues.* Nature, 2017. **542**(7642): p. 450–455.
40. Cheng, Y. and W. Liu, *MicroRNA-503 serves an oncogenic role in retinoblastoma progression by directly targeting PTPN12.* Exp Ther Med, 2019. **18**(3): p. 2285–2292.
41. Li, L., et al., *MiR-503 promotes the migration and invasion of colorectal cancer cells by regulating PDCD4.* J buon, 2018. **23**(3): p. 579–586.
42. Montfort, A., et al., *A Strong B-cell Response Is Part of the Immune Landscape in Human High-Grade Serous Ovarian Metastases.* Clin Cancer Res, 2017. **23**(1): p. 250–262.
43. Bassani, B., et al., *Natural Killer Cells as Key Players of Tumor Progression and Angiogenesis: Old and Novel Tools to Divert Their Pro-Tumor Activities into Potent Anti-Tumor Effects.* Cancers (Basel), 2019. **11**(4).
44. Dean, I., et al., *Rapid functional impairment of natural killer cells following tumor entry limits anti-tumor immunity.* Nat Commun, 2024. **15**(1): p. 683.
45. Rosser, E.C. and C. Mauri, *Regulatory B cells: origin, phenotype, and function.* Immunity, 2015. **42**(4): p. 607–12.
46. Zhang, E., et al., *Roles and mechanisms of tumour-infiltrating B cells in human cancer: a new force in immunotherapy.* Biomark Res, 2023. **11**(1): p. 28.
47. McCool, K.W., et al., *Murine Oviductal High-Grade Serous Carcinomas Mirror the Genomic Alterations, Gene Expression Profiles, and Immune Microenvironment of Their Human Counterparts.* Cancer Res, 2020. **80**(4): p. 877–889.
48. Zhai, Y., et al., *High-grade serous carcinomas arise in the mouse oviduct via defects linked to the human disease.* J Pathol, 2017. **243**(1): p. 16–25.
49. Ewels, P.A., et al., *The nf-core framework for community-curated bioinformatics pipelines.* Nat Biotechnol, 2020. **38**(3): p. 276–278.
50. Kechin, A., et al., *cutPrimers: A New Tool for Accurate Cutting of Primers from Reads of Targeted Next Generation Sequencing.* J Comput Biol, 2017. **24**(11): p. 1138–1143.
51. sclamons, F.K.F.J.P.E.E.A.M.W.B.S.-B.G.H., *FelixKrueger/TrimGalore: v0.6.10 - add default decompression path.* 2023.
52. Dobin, A., et al., *STAR: ultrafast universal RNA-seq aligner.* Bioinformatics, 2013. **29**(1): p. 15–21.
53. Patro, R., et al., *Salmon provides fast and bias-aware quantification of transcript expression.* Nat Methods, 2017. **14**(4): p. 417–419.

54. Soneson, C., M.I. Love, and M.D. Robinson, *Differential analyses for RNA-seq: transcript-level estimates improve gene-level inferences.* F1000Res, 2015. **4**: p. 1521.
55. Robinson, M.D., D.J. McCarthy, and G.K. Smyth, *edgeR: a Bioconductor package for differential expression analysis of digital gene expression data.* Bioinformatics, 2010. **26**(1): p. 139–40.
56. Ritchie, M.E., et al., *limma powers differential expression analyses for RNA-sequencing and microarray studies.* Nucleic Acids Res, 2015. **43**(7): p. e47.
57. Korotkevich, G., et al., *Fast gene set enrichment analysis.* bioRxiv, 2021: p. 060012.
58. Liberzon, A., et al., *Molecular signatures database (MSigDB) 3.0.* Bioinformatics, 2011. **27**(12): p. 1739–40.
59. Walton, J., et al., *CRISPR/Cas9-Mediated Trp53 and Brca2 Knockout to Generate Improved Murine Models of Ovarian High-Grade Serous Carcinoma.* Cancer Res, 2016. **76**(20): p. 6118–6129.
60. Nguyen, L.L., et al., *EHMT1/2 inhibition promotes regression of therapy-resistant ovarian cancer tumors in a CD8 T cell-dependent manner.* Mol Cancer Res, 2024.
61. Yamamoto, T.M., et al., *Activation of Wnt signaling promotes olaparib resistant ovarian cancer.* Mol Carcinog, 2019.
62. *nf-core/rnaseq: nf-core/rnaseq v3.14.0 - Hassium Honey Badger.* 2024.

ACKNOWLEDGMENTS:

Ethics approval and consent to participate: All mouse studies were approved by the University of Colorado Institutional Animal Care and Use Committee (IACUC; protocols 157 [generation of HSCDA-Pro and HSCDA-Def mice] and 569 [syngeneic models of ovarian cancer]). The samples utilized for primary preadipocyte culture were obtained under approval by the Colorado Multiple Institutional Review Board (COMIRB) with written informed consent from all participants. Samples were obtained from participants enrolled in NCT02654925, NCT04043520, and NCT03396978 and shared in a de-identified manner as secondary use in this investigation as approved by COMIRB #22-0809.

Consent for publication: N/A

Availability of data and materials: Data generated and/or analyzed during this study are available from the corresponding author upon reasonable request. RNA-Seq or other large datasets are deposited as described in Materials and Methods and are publicly available.

Conflict of interests: The authors declare that they have no conflict of interest.

Funding: ZLW is a Scholar of the Colorado Specialized Center for Research Excellence (CO-SCORE) on Sex Differences (U54 AG062319) focused on Bioenergetic and Cardiometabolic Consequences of the Loss of Gonadal Function. This work was primarily supported by the Department of Defense Ovarian Cancer Research Program (ZLW, OC210257; SO, HT94252410193) and the Colorado Clinical & Translational Sciences Institute (ZLW, CCTSI CO-Pilot CO-J-20-006), with additional support by the merged Ovarian Cancer Research Alliance / Rivkin Center for Ovarian Cancer Research (ZLW, Pilot Award RPG-R-2024-2-1269446) as well as Institutional Research Grant #22-154-59 from the American Cancer Society to the University of Colorado Cancer Center (ZLW). Further support was provided by the American Cancer Society (BGB, RSG-19-129-01-DDC), the NCI (BGB, R37CA261987; ZLW, R03CA249571), NIDDK (KMG, K01DK109053), NIA (KMG and DJK, U54 AG062319), the VA (SO, I01BX006020), and the Boettcher Foundation. Use of the University of Colorado Bioinformatics and Biostatistics Shared Resource (BBSR), Human Immune Monitoring Shared Resource (HIMSR), and the Cell Technologies Shared Resource (CTSR) was supported by NCI grant P30CA046934 and by NIH/NCATS Colorado CTSA grant UL1TR002535. This work was supported by the Alpine HPC system, which is jointly funded by the University of Colorado Boulder, the University of Colorado Anschutz, Colorado State University, and the National Science Foundation (award 2201538).

Author's contributions:

ERW (co-first author): performed experiments, analyzed data, prepared manuscript

CAB (co-first author): performed experiments, analyzed data, prepared manuscript

FT (co-first author): performed experiments, analyzed data, revised manuscript

VM: performed experiments, analyzed data

JKM: performed experiments

TMS: performed experiments

MPB: analyzed data, revised manuscript

MSR: provided study materials

RV: provided study materials, aided in study design

BC: provided study materials, revised manuscript

KRJ: analyzed data

KMG: provided study materials, aided in study design, revised manuscript

DJK: provided study materials, aided in study design

SO: provided study materials

BGB: provided study materials, aided in study design, data analysis and interpretation, revised manuscript

ZLW: designed the study, performed experiments, analyzed and interpreted data, prepared manuscript

Additional Acknowledgments: The authors acknowledge with extensive gratitude the anonymous donors who provided biopsies for use in generating adipocyte cultures. We acknowledge philanthropic contributions from the Kay L. Dunton Endowed Memorial Professorship in Ovarian Cancer Research, the McClintock-Addlesperger Family, Karen M. Jennison, Don and Arlene Mohler Johnson Family, Michael Intagliata, Duane and Denise Suess, Mary Normandin, and Donald Engelstad. The corresponding author (Zachary L Watson) wishes to dedicate this manuscript in memory of Maggie Watson (1981-2022) and Mira Watson (2016-2022).

FIGURES:

Woodruff, Bailey, and To et al. - Fig. 1

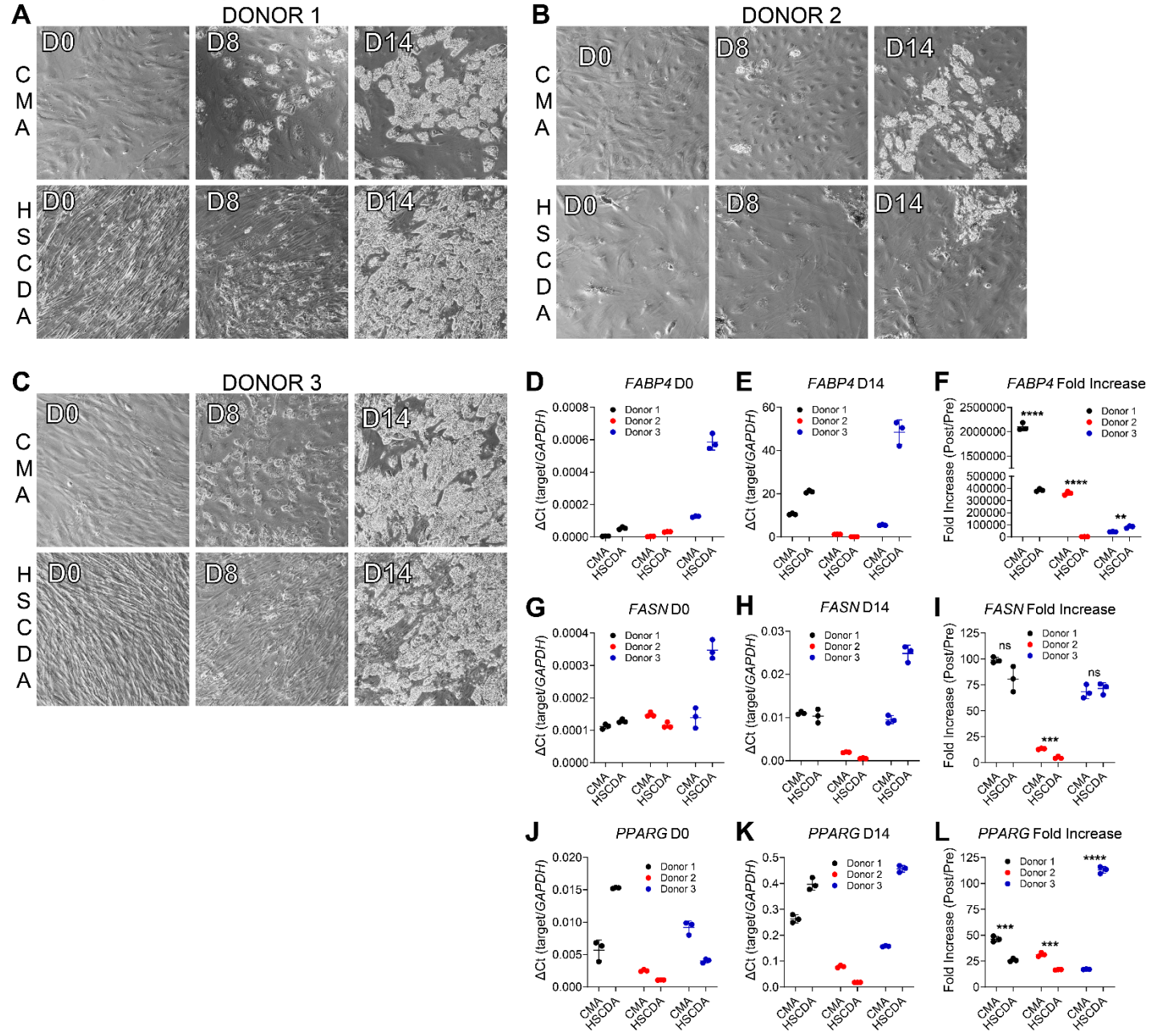

Fig. 1. Human hematopoietic and mesenchymal precursors undergo similar adipogenic differentiation *in vitro*. (A-C) Brightfield images of cells from human female Donors 1-3 as they progress from confluent pre-differentiated precursor cells (D0) through mid-differentiation and appearance of lipid droplets (D8) to post-differentiation (D14). Paired mesenchymal precursor/CMAs and hematopoietic/HSCDAs are shown. **(D-L)** Confluent human precursor cells (D0, **D, G, J**) and fully differentiated HSCDAs and CMAs (D14, **E, H, K**) were analyzed by RT-qPCR for mRNA expression of *FABP4*, *FASN*, and *PPARG*. Expression was normalized by ΔCt to *GAPDH*. Fold increases in each gene were plotted by dividing D14/D0 expression (**H, K, N**). Triplicate data

points are plotted along with mean ± SD. For fold increases, p-values are calculated by unpaired t-test. **$p<0.01$, ***$p<0.001$, ****$p<0.0001$, ns=not significant.

Woodruff, Bailey, and To et al. - Fig. 2

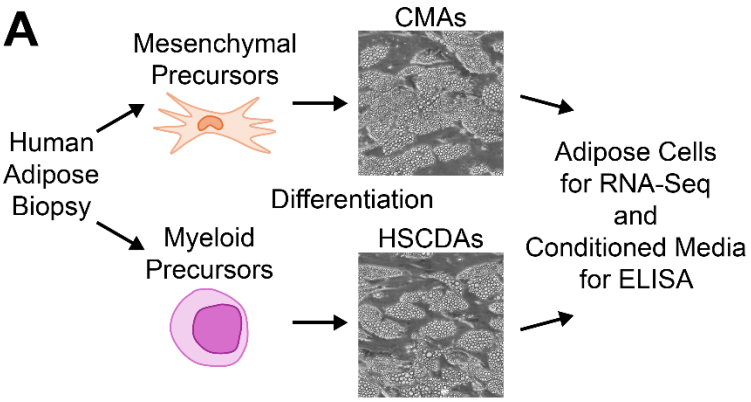

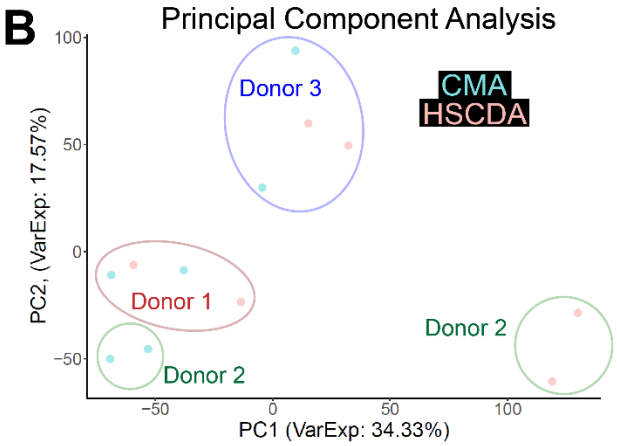

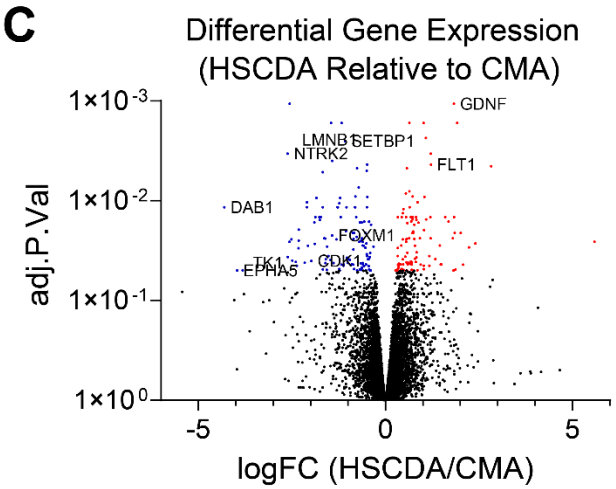

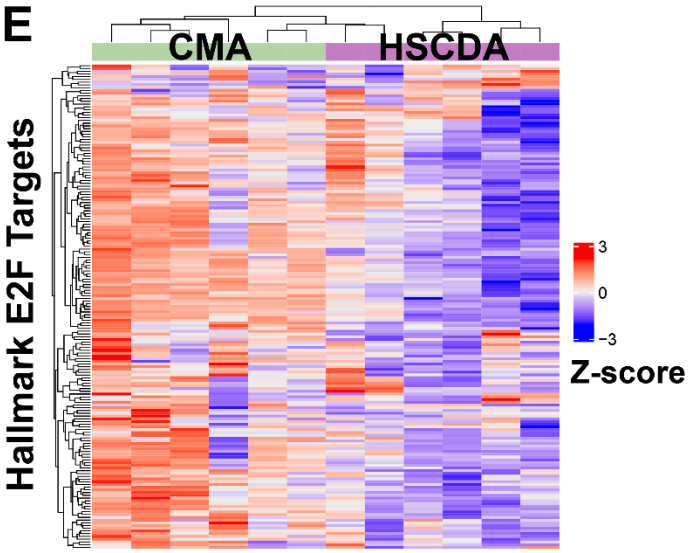

D

Hallmark ID	No. genes / Input genes	qvalue
E2F Targets	17 / 90	0.00011
Mitotic Spindle	16 / 90	0.00048
G2M Checkpoint	14 / 90	0.00211

F

HALLMARK ID	padj	NES
P53_PATHWAY	0.000279736	1.830789521
XENOBIOTIC_METABOLISM	0.000279736	1.958151026
G2M_CHECKPOINT	0.000279736	-2.438546753
E2F_TARGETS	0.000279736	-2.290562385
MITOTIC_SPINDLE	0.001568979	-1.702521627
HYPOXIA	0.002414453	1.668657889
OXIDATIVE_PHOSPHORYLATION	0.00668037	1.571744257
ESTROGEN_RESPONSE_EARLY	0.018521217	1.542840882
APICAL_JUNCTION	0.018521217	1.547290794
TNFA_SIGNALING_VIA_NFKB	0.02326929	1.506083461
ADIPOGENESIS	0.025052397	1.467282689
FATTY_ACID_METABOLISM	0.035019763	1.491172164

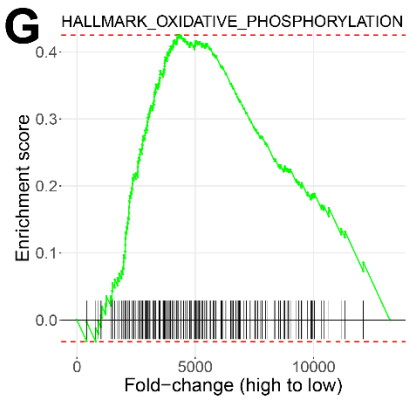

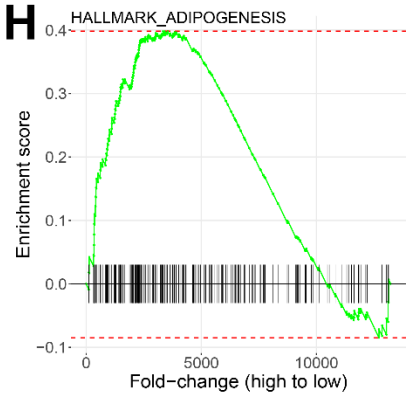

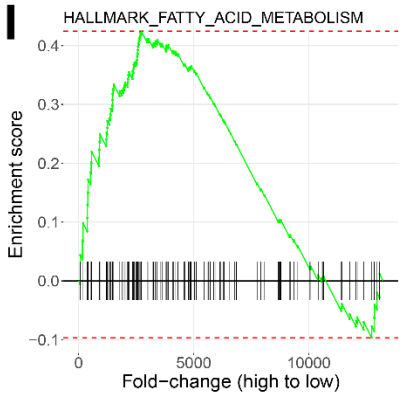

Fig. 2. *In vitro* differentiated human primary HSCDAs exhibit unique transcription relative to CMAs. (A) Diagram of adipogenic differentiation of human primary precursor cells into HSCDAs and CMAs. Cell transcriptomes were analyzed in duplicate by RNA-Seq. **(B)** Principal component analysis (PCA) of adipocyte RNA-Seq. **(C)** Volcano plot of differential gene expression (DGE) comparing HSCDAs relative to CMAs. Specific gene names in E2F and other pathways are highlighted. **(D)** Significantly differentially regulated hallmark pathways by over-representation analysis (ORA). **(E)** Heatmap of Hallmark E2F Targets showing transcriptional downregulation of the pathway in HSCDAs relative to CMAs. **(F)** Hallmark pathways were significantly enriched in functional gene set enrichment analysis (fGSEA). padj = p value adjusted for multiple comparisons. NES = Normalized Enrichment Score. A positive NES indicates over-enrichment of pathway genes in HSCDAs relative to CMAs, while a negative NES indicates under-enrichment in HSCDAs relative to CMAs. Note the negative NES values for the hallmark pathways shown by ORA in **D**, confirming downregulation of these pathways in HSCDAs. **(G-I)** fGSEA plots corresponding to the indicated Hallmark metabolic pathways in **F**. The peak-shaped plots correspond to the positive NES and indicate over-enrichment in HSCDAs relative to CMAs.

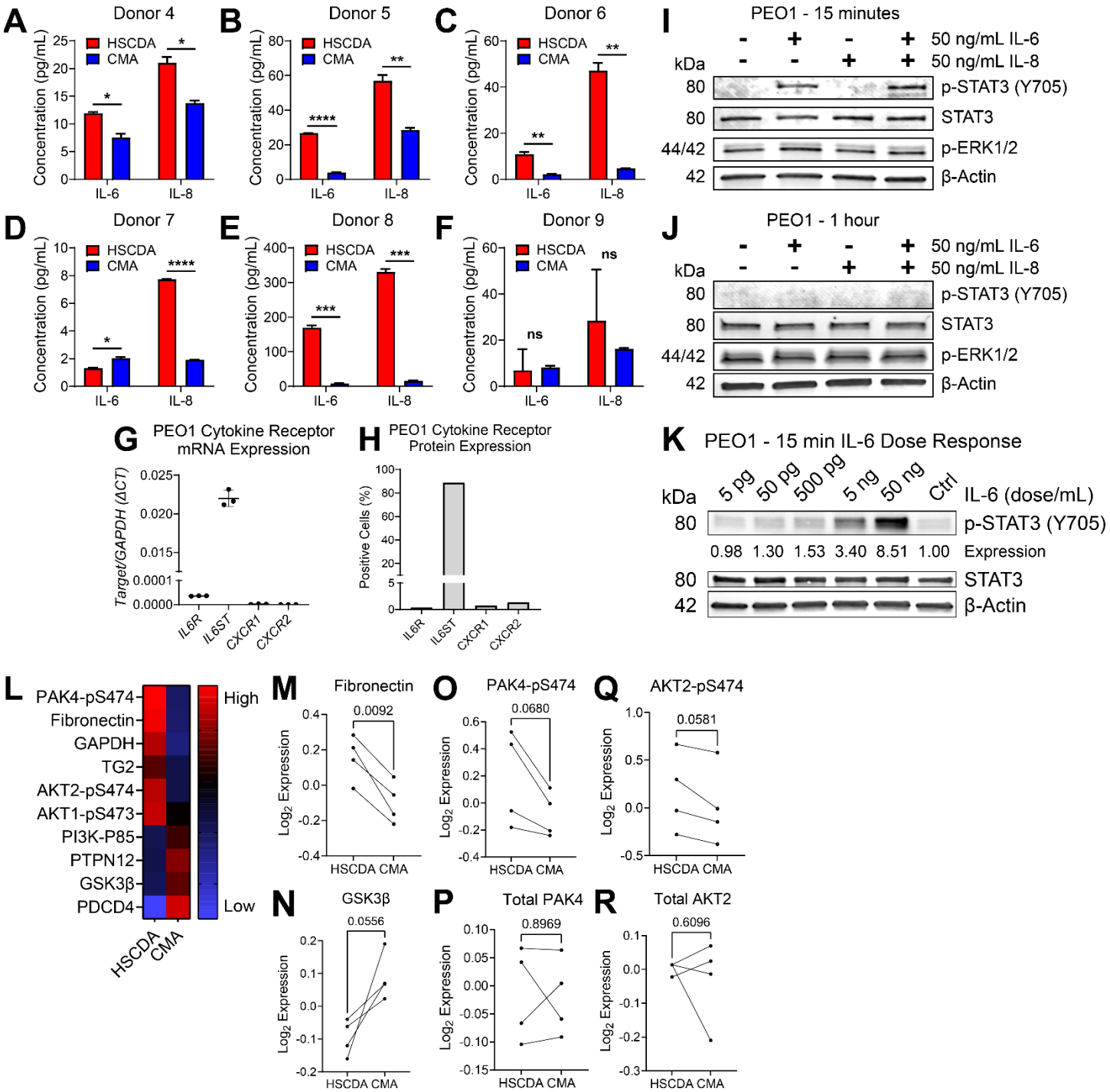

Fig. 3. *In vitro* differentiated human primary HSCDAs secrete greater amounts of IL-6 and IL-8 than CMAs. **(A-F)** HSCDA or CMA conditioned media from six independent human donors was examined by ELISA for IL-6 and IL-8. Data are plotted as mean ± SD of two wells. Unpaired t-test. * $p<0.05$, ** $p<0.01$, *** $p<0.001$, **** $p<0.0001$. **(G)** RNA was isolated from PEO1 cells and RT-qPCR was performed for the indicated cytokine receptor transcripts. *GAPDH* was used for ΔCt quantification. **(H)** Flow cytometry was performed on PEO1 cells to detect surface expression of the indicated cytokine receptor proteins. **(I-K)** PEO1 cells were incubated with

the indicated cytokine supplements for the indicated time. Immunoblots were performed for phosphorylated and total STAT3 (IL-6 signaling), phosphorylated ERK1/2 (IL-8 signaling), and β-actin loading control. **(L-R)** PEO1 cells were incubated in conditioned media from HSCDAs or CMAs for 24 hours. Protein expression and phosphorylation were examined by RPPA. **(L)** The heat map shows the average median centered Log2 expression for PEO1 cells incubated in 4 independent media pairs (Donors 6 through 9). **(M-N)** Representative paired scatter plots showing consistent differential protein expression of fibronectin and GSK3β in PEO1 cells incubated in each media pair. **(O-R)** Paired scatter plots for phosphorylated and total forms of PAK4 and AKT2, showing differential regulation of serine phosphorylation, but not total protein. P-values by paired t-test.

Woodruff, Bailey, and To et al. - Fig. 4

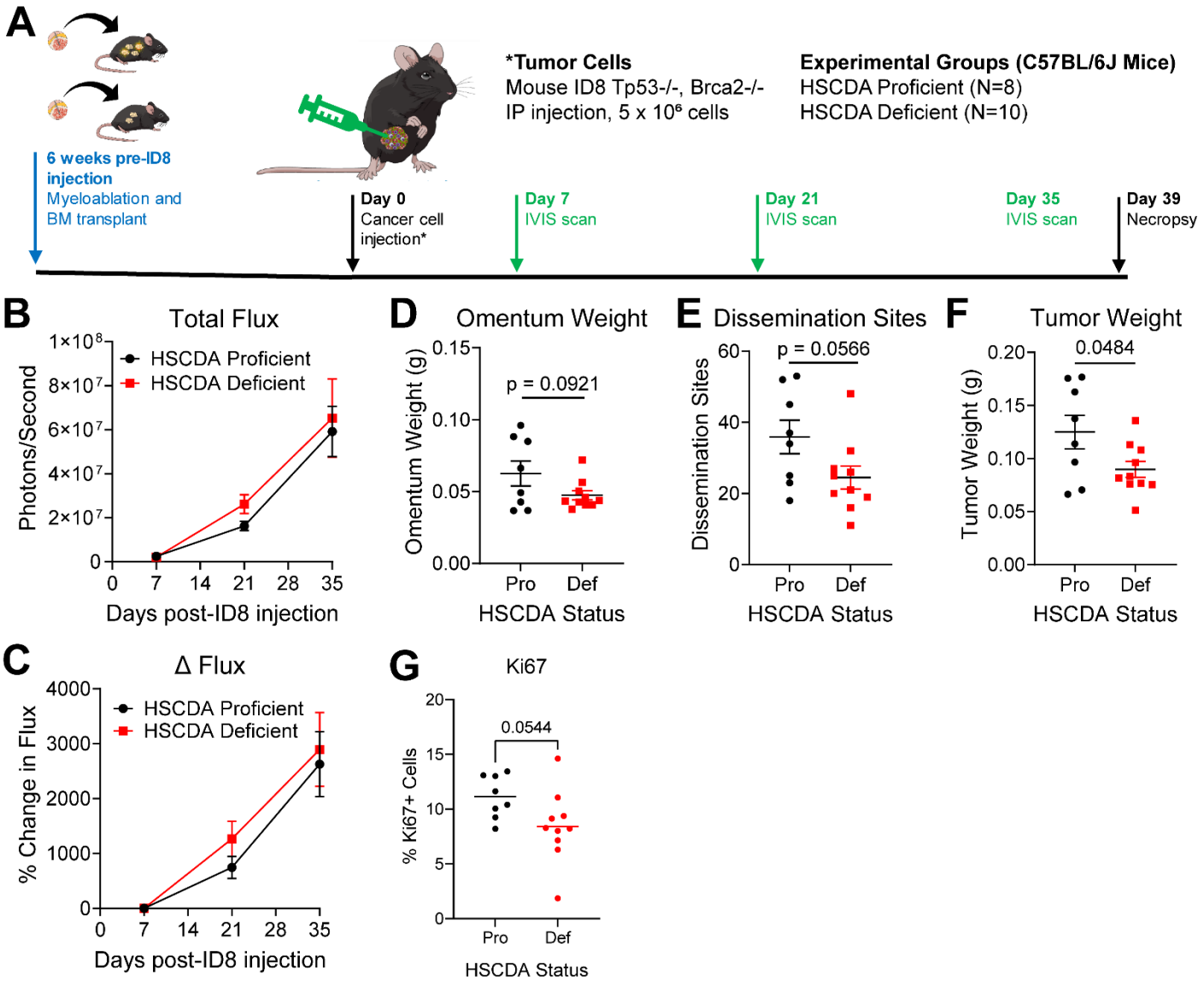

Fig. 4. Ablation of HSCDAs reduces tumor burden in the ID8 syngeneic mouse model of HGSC. (A) Experimental timeline, including bone marrow transplant and subsequent tumor study. **(B)** Total flux and **(C)** percent change in total flux (relative to 7 days post-ID8 injection) by luciferase live imaging. **(D)** Weight of omental tumors. **(E)** Number of disseminated tumor nodules. **(F)** Weight of disseminated tumor nodules. For **(D-F)**, graphs show individual data points with mean ± SEM. p-values by unpaired T-test. **(G)** The percentage of Ki67-positive tumor cells was determined using QuPath software (representative images are shown in **Supplementary Fig. S9**). For **(G)**, individual data points with means (horizontal bar). p-values by unpaired T-test. Pro = HSCDA-Pro; Def = HSCDA-Def.

Woodruff, Bailey, and To et al. - Fig. 5

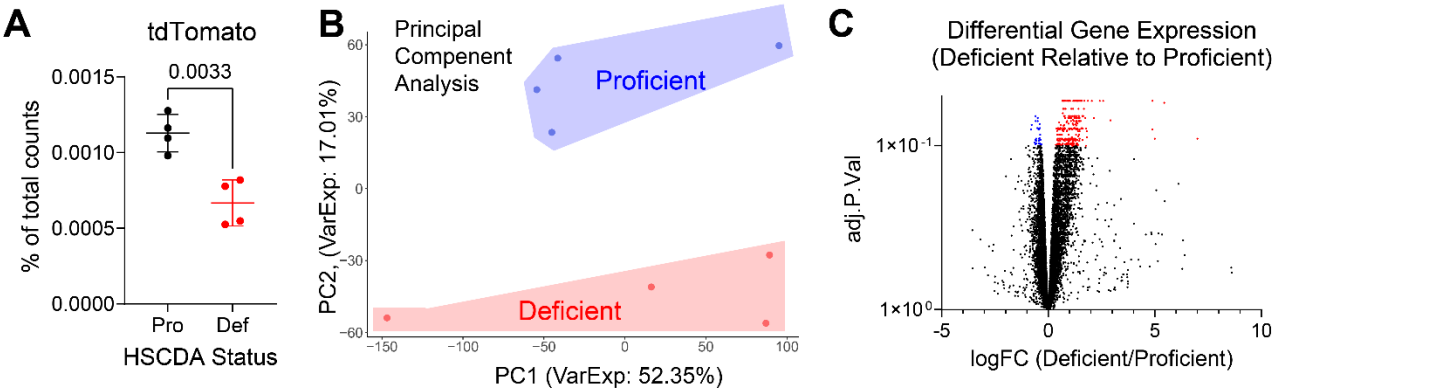

D

HALLMARK ID	padj	NES
XENOBIOTIC_METABOLISM	0.006754	-1.6101
ALLOGRAFT_REJECTION	0.006754	-2.1533
KRAS_SIGNALING_UP	0.006754	-1.60267
EPITHELIAL_MESENCHYMAL_TRANSITION	0.006754	-1.69105
FATTY_ACID_METABOLISM	0.006754	-1.59835
OXIDATIVE_PHOSPHORYLATION	0.006754	-1.97444
NOTCH_SIGNALING	0.006754	-1.98139
ADIPOGENESIS	0.009559	-1.50634
PROTEIN_SECRETION	0.009559	-1.61366
UV_RESPONSE_DN	0.015571	-1.54007
INFLAMMATORY_RESPONSE	0.015605	-1.45088
MYC_TARGETS_V1	0.015605	-1.38771
IL2_STAT5_SIGNALING	0.018997	-1.39293
APOPTOSIS	0.018997	-1.46009
COAGULATION	0.020379	-1.4758
TGF_BETA_SIGNALING	0.021282	-1.64548
BILE_ACID_METABOLISM	0.021282	-1.52442
KRAS_SIGNALING_DN	0.021617	1.524156
PANCREAS_BETA_CELLS	0.021617	-1.79148
APICAL_JUNCTION	0.030503	-1.33646

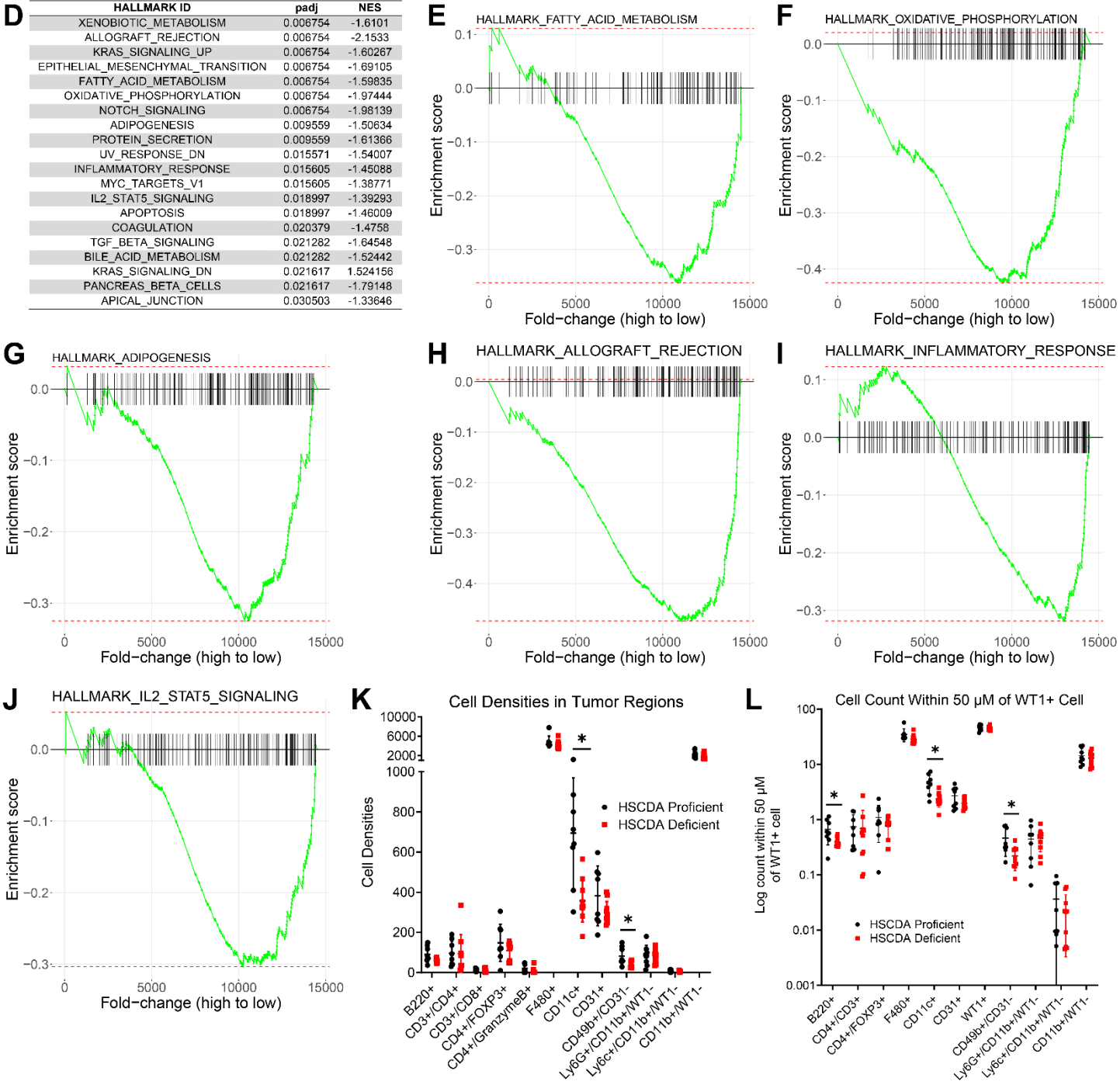

Fig. 5. Ablation of HSCDAs in mice alters ID8 omental tumor gene transcription and the tumor immune microenvironment. (A) tdTomato (exogenous transgene from bone marrow donor cells) expression in ID8 omental tumor RNA-Seq from HSCDA-Pro (n=4) and HSCDA-Def (n=4) mice, expressed as percentage of total counts. Error bars = mean ± SD. Unpaired T-test. **(B)** Principal component analysis. **(C)** Differential gene expression volcano plot of overall RNA-Seq gene expression in HSCDA-Def mice relative to HSCDA-Pro mice (i.e., positive values indicate greater expression in HSCDA-Def mice). **(D)** Significantly differentially regulated hallmark pathways by fGSEA. padj = p value adjusted for multiple comparisons. NES = Normalized Enrichment Score (adjusted for multiple comparisons). A positive NES indicates over-enrichment of pathway genes in HSCDA-Def mice relative to HSCDA-Pro mice, while a negative NES indicates under-enrichment in HSCDA-Def mice relative to HSCDA-Pro. **(E-G)** fGSEA enrichment plots for hallmark metabolic pathways. **(H-J)** fGSEA enrichment plots for hallmark immune pathways. The U-shaped plots in **E-J** correspond to negative NES in **D**. **(K)** Quantification of cell densities in omental tumors. **(L)** Quantification of the number of the indicated immune cells within 50 microns of a WT1+ tumor cell. Error bars = SD. Unpaired T-test. * $p<0.05$.

TABLES:

Table 1: Adipose Donor Characteristics

Donor ID	Age	Menopause	Height (cm)	Fat mass (kg)	Total mass (kg)	Relative fat mass (%)
1	52	Post	173	32	79	41
2	53	Post	180	41	90	46
3	56	Post	157	16	50	31
4	33	Pre	165	33	83	40
5	26	Pre	157	30	77	39
6	54	Post	170	20	58	34
7	52	Post	160	29	73	40
8	53	Post	168	50	111	45
9	61	Post	173	34	83	41

Table 2: Multispectral IHC Antibody Panel for Innate/Myeloid Mouse Immune Cells

Antibody	Marker Expression
CD11b	Myeloid cells
CD11c	Dendritic cells
Ly6c	Monocytic MDSCs
Ly6g	Granulocytic MDSCs
CD49b	NK and endothelial cells
CD31	Endothelial cells
F4/80	Macrophages
WT1	ID8 tumor cells
DAPI	Nuclei

Table 3: Multiplex IHC Antibody Panel for Adaptive/Lymphoid Mouse Immune Cells

Antibody	Marker Expression
CD3	T-cells
CD4	Helper T-cells
CD8	Cytotoxic T-cells
Granzyme B	Effector T-cells
FOXP3	Regulatory T-cells
B220	B-cells
WT1	ID8 tumor cells
DAPI	Nuclei

SUPPLEMENTARY MATERIALS:

Supplementary Figures S1 – S11

Supplementary Tables ST1 – ST5

The supplementary materials are prepared as a separate file as required by the instructions for authors.